Green and Sustainable Environments

Green and Sustainable Environments **1** (2026) 11
https://doi.org/10.62755/gsenv.2026.11
journal homepage: pubs.greensus.org/gsenv

Check for updates



RESEARCH PAPERS

Hydrothermal Carbonization of Cane Molasses as a Waste-Valorization Route: Product Recovery, Structure, and the Limits of Adsorption Assessment

Sephia Amanda Muhtar[1,†], Kamilah Nada Maisa[2], Kholik Hidayatullah[2], Abdul Latief Salim Azpar[3], Alam Hannaan Muhammad[3], Panji Setyo Nugroho[2], Andika Munandar[1,*]

[1] Department of Environmental Engineering, Faculty of Infrastructure and Regional Technology, Institut Teknologi Sumatera, Terusan Ryacudu, Way Hui, Jati Agung, Lampung Selatan 35365, Indonesia
[2] Department of Physics, Faculty of Mathematics and Natural Sciences, Institut Teknologi Bandung, Jalan Ganesa 10, Bandung 40132, Indonesia
[3] Department of Environmental Engineering, Faculty of Civil and Environmental Engineering, Institut Teknologi Bandung, Jalan Ganesa 10, Bandung 40132, Indonesia
[†] Present address (S. A. Muhtar): Institut Teknologi Bandung, Jalan Ganesa 10, Bandung 40132, Indonesia

* **Corresponding author**: andika.munandar@tl.itera.ac.id

ARTICLE HISTORY: Received: September 9, 2026 · Revised: November 22, 2026 · Accepted: November 22, 2026

ABSTRACT

Cane molasses, the residual syrup of sugar manufacture, is mostly fermented, a route that returns a high-strength effluent; hydrothermal carbonization can convert it directly to a solid. Hydrochars are commonly assessed as adsorbents by fitting kinetic and isotherm models, often without checking that the measured concentrations lie within the analytical calibration. We prepared hydrochars from 10, 15, and 20 g molasses in 50 mL water at 140 °C for 24 h and examined product recovery, bulk structure, and the analytical validity of an ammonium adsorption dataset. Wet-feed yield increased from $(11.74 \pm 1.10)\,\%$ ($n = 5$) at 10 g to $(17.49 \pm 1.30)\,\%$ ($n = 4$) and $(18.38 \pm 2.03)\,\%$ ($n = 3$) at 15 and 20 g ($\rho = 0.834$, $p = 0.00074$), although loading and production date were not balanced. The three products had closely matching infrared spectra and X-ray diffraction patterns ($r = 0.997$–0.998), dominated by an amorphous carbon envelope, but anhydrite ($CaSO_4$) appeared in the 20 g product alone: the series differs in feed-derived mineral content rather than in carbon structure. Infrared band ratios separated the 10 h from the 24 h products, toward greater carbonyl and C–O absorbance after 24 h. The ammonium measurements, made on the products after a 400 °C treatment in air, lay above the 1–5 mg L^{-1} Nessler calibration in all 66 contact-time and 36 of 42 concentration-series samples, and neither a lost dilution nor a change of concentration basis reconciles them. These data establish hydrochar recovery and structural similarity across the loading series, but not ammonium capacity, kinetics, or isotherms. A calibration-range test applied before model fitting separates the adsorption claims a hydrochar dataset can carry from those it cannot.

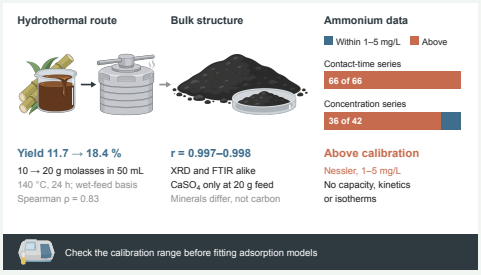

KEYWORDS *molasses; hydrothermal carbonization; waste valorization; ammonium; adsorption; analytical validation*

1. INTRODUCTION

Cane sugar manufacture leaves molasses, the syrup that remains once further sucrose can no longer be crystallized economically. Its composition varies widely between mills and cane sources: across 16 cane molasses samples sourced worldwide, sucrose spanned 39.2–67.3 % of dry matter and the inorganic residue averaged 13.1 % of dry matter [1]. Molasses is used as an animal feed and as a fermentation substrate for ethanol, yeast, and amino acids. World output is estimated at 55 million tonnes per year [2]. The fermentation route returns a spent wash whose organic load, low pH, and dark color place it among the more difficult industrial effluents to treat, and inadequately treated discharge from cane sugar and distillery operations is a documented source of soil and water pollution in producing regions [3]. Converting molasses directly into a solid carbon material is an outlet that does not pass through that effluent.

Hydrothermal carbonization (HTC) converts an aqueous biomass feed into a carbon-rich solid under autogenous pressure at temperatures commonly below those used for pyrolysis [4]. The route suits a wet feed such as molasses because no drying is required before conversion. Sugars dehydrate, condense, and polymerize in the liquid phase and form predominantly amorphous carbon micro- or nanospheres [5, 6]. Yield and surface chemistry depend on the feedstock, the solid-to-water ratio, temperature, and residence time, so each has to be separated from any performance the product is later credited with [7–9]. Recent work on molasses and sugar-industry residues has varied mainly the reaction temperature, additives, and activation. Date-palm molasses carbonized at 180 to 250 °C gave carbon microspheres in up to 40.4 % yield but with Brunauer–Emmett–Teller (BET) areas below 1 $m^2\,g^{-1}$ [10], and porous products were obtained only after phosphoric acid activation [11] or with ferrate and iron additives [12]. Cane molasses has also served as the carbon source for a magnetic amino-functional material [13], while press mud and bagasse hydrochars have been assessed as fuels and soil amendments [14] or activated for pesticide removal [15, 16]. How the charge of feed into a fixed water volume governs recovery, which sets the material balance of a valorization route, has received less attention.

Ammonium reaches surface water through municipal and industrial effluents, landfill leachate, and agricultural runoff. At elevated loads it contributes to eutrophication and the associated loss of water quality and ecosystem function [17, 18]. Adsorption is attractive as a polishing step because it is simple to operate and can treat dilute streams, and hydrochars from agricultural and industrial residues have been tested against metals and nutrient ions on that basis [19, 20]. Unmodified hydrochars from sugarcane bagasse and leaves have taken up about 3 to 20 mg g^{-1} ammonium [21, 22], and a paper-sludge hydrochar about 20 mg g^{-1} [23]. Ammonium uptake by chars does not follow surface area alone: surface functional groups, ash composition, pH, and cation-exchange properties can be equally important [20, 24, 25], and competing Mg^{2+} and K^+ halved the uptake of a sugarcane hydrochar in digestate [22]. A loading series can thus change mass recovery, bulk structure, and surface affinity by different amounts, and the three have to be established separately.

Two questions follow, and they are of different kinds. The first is chemical: whether changing how much molasses is charged into a fixed water volume changes the solid that forms, or only how much of it is

e-ISSN 3124-4610 · © 2026 The Authors · CC BY 4.0 OPEN ACCESS

recovered. The second is evidential. Adsorption performance is often reported in a form that cannot be checked against the measurement behind it. A critical review of the field documents recurring problems with the quantities used to express performance, with kinetic and isotherm fitting, and with data points that are inconsistent between experiment and model [26], and the apparent dominance of the pseudo-second-order rate law has been traced to modeling conventions that favor it rather than to the kinetics of the systems it is fitted to [27]. Recent hydrochar studies still select isotherms by R^2 from linearized fits [21, 28], although the analytical basis can be documented directly, by diluting samples into the calibration interval [29] or validating the method over the working range [15]. Capacities and rate constants can otherwise be carried to three figures from absorbances whose analytical basis was never established.

We compared 10, 15, and 20 g molasses in a fixed 50 mL water volume, characterized the solids, and measured ammonium uptake as a function of contact time and initial concentration, working throughout from the complete batch record and the raw spectroscopic and adsorption measurements rather than from summary values. The characterization answers the first question and separates the part of the product that loading changes from the part it does not. The second question is answered in the negative: we report the analytical boundary that produces that answer, and the measurements needed to cross it, rather than nominal capacities computed beyond it.

2. MATERIALS AND METHODS

2.1 Materials

Molasses was collected from the Cinta Manis sugar factory in Ogan Ilir, South Sumatra, Indonesia, and used as received without filtration or dilution. Ammonium chloride (analytical grade, ≥99.5 %), ethanol (96 %), and a ready-to-use Nessler reagent solution were obtained from Merck (Darmstadt, Germany) and used as received. Deionized water was used for all syntheses, washing steps, and solutions. No acid, base, or buffer was added at any stage. Samples were filtered through 0.45 µm polytetrafluoroethylene (PTFE) syringe filters before analysis.

2.2 Hydrochar Preparation

Molasses feed of 10, 15, or 20 g was mixed with 50 mL deionized water in a 100 mL beaker. The mixture was transferred to a PTFE-lined reactor and held at 140 °C for 24 h. The resulting suspension was recovered under vacuum, washed with ethanol and water, and dried at 80 °C for 12 h. Hydrochar yield was calculated on the as-received molasses mass basis,

$$Y = \frac{m_{\mathrm{hydrochar}}}{m_{\mathrm{molasses}}} \times 100\,\%. \tag{1}$$

The 24 h hydrochars are denoted MH10, MH15, and MH20 after the molasses feed mass.

A second series was prepared at 140 °C for 10 h and is compared with the 24 h products in Section 3.3. Only its temperature and residence time were recorded; whether it passed through the same mixing, washing, and drying steps was not.

A portion of the product from each feed loading was then heated in a covered crucible in air at 10 °C min^{-1} to 400 °C and held for 2 h; this treated fraction, denoted MH10-400, MH15-400, and MH20-400, was the adsorbent used in the ammonium experiments. Its mass after treatment was not measured, and the treated material was not characterized: the characterization data in Section 3 describe the products before this step. Heating hydrochar in air at 300 to 450 °C is a common activation step that adds oxygen-containing surface groups [30] and, toward the upper end of that range, burns off carbon and enriches the ash [31]. The route, and the measurement each product received, are summarized in Fig. 1.

2.3 Material Characterization

Fourier-transform infrared (FTIR) spectra were recorded on a Shimadzu IRSpirit spectrometer through a single-reflection diamond attenuated-total-reflection accessory, over 401.6–3998.8 cm^{-1} at 628 points, giving a sampling interval of 5.737 cm^{-1}, at 4 cm^{-1} resolution with 45 accumulations and Happ–Genzel apodization. Six spectra were measured consecutively in one session: three from the 10 h products and three from the 24 h products. On export the instrument software adds a constant per-sample transmittance offset, between +2.14 and −4.37 %, which places two of the six above 100 % transmittance; the unshifted ordinates were used throughout. Band positions were taken as minima of the second derivative [32], computed with a third-order Savitzky–Golay filter [33] over nine points and interpolated parabolically, and were accepted above five times the derivative noise of each spectrum, measured in the 3700–3990 cm^{-1} blank region. A band is reported for a series when it is resolved in at least two of its three spectra. The 1850–2500 cm^{-1} interval, which carries the diamond two-phonon absorption and the atmospheric CO_2 doublet, is excluded throughout. Because attenuated-total-reflection absorbance scales with contact pressure, spectra are compared between samples only as ratios to the 1610 cm^{-1} band.

X-ray diffraction (XRD) patterns were collected on a PANalytical diffractometer in a spinner reflection–transmission configuration with Cu Kα_1 radiation (1.540 598 Å) over 5.05–80.00° 2θ, at 31.115 s per step and about 6.4 min per scan, all six on 4 July 2023. Patterns were smoothed over 41 points and standardized before pairwise Pearson correlations were calculated.

Crystalline reflections were separated from the amorphous scattering before phase identification. The broad background was estimated by iterative SNIP clipping [34] and subtracted, and maxima in the residual were retained when they exceeded four times the local noise, cleared a prominence threshold, and had a full width at half maximum below 1.5° measured above the local background. Retained reflections were matched against the experimental cards of the PDF-2 powder diffraction file [35]; a phase was accepted only when its strongest line and its strong companions were all present as detected reflections with intensity ratios consistent with the card [36]. Whewellite and calcite were carried as negative controls. The identification is qualitative, and no weight fractions are reported. The amorphous band was characterized separately by fitting a Gaussian on a linear background over 12–32° 2θ, with 24.6–26.2° excluded so that the superimposed crystalline reflection could not bias the position or width; interlayer spacing follows from the fitted center through the Bragg relation and apparent stack height from the Scherrer equation [37] with $K = 0.9$, both without instrumental broadening correction.

Surface morphology and elemental composition were examined on a Thermo Fisher Quattro scanning electron microscope with an Everhart–Thornley detector in secondary-electron mode at 10.00 kV, spot size 2.5, and working distances of 10.6–12.6 mm, coupled to a Bruker energy-dispersive X-ray spectrometer operated in mapping mode. Micrographs were taken at five carbonization temperatures, 140, 175, 180, 200, and 220 °C, each at 1000×, 5000×, and 10000×, with one spectrometer report per temperature; all were acquired on 3 March 2023, with a 220 °C repeat on 8 March. The samples were examined uncoated, so the carbon signal in the spectrometer reports is from the hydrochar itself. The spectra were digitized from the instrument plots, with the energy axis calibrated from the minor tick marks and verified against the oxygen Kα maximum, which lands within 0.02 keV of its reference position in all six. Characteristic lines were measured as the integrated excess over a local linear baseline, in units of the scatter in the two flanking windows, with potassium Kα, calcium Kβ, and a blank window at 5.5 keV as controls.

Sample identities follow the labels the measurements themselves carry. Spectra h1024, h1524, and h2024 are taken as the 24 h products from the 10, 15, and 20 g feeds, and H10, H15, and h20 as the corresponding 10 h products; the acquisition order places the 10 h set immediately before the 24 h set within the single session. Diffraction patterns HD, HE, and HF are assigned to the same loading sequence. These assignments are provisional, since no independent sample list accompanies the measurements. Three further patterns, HA, HB, and HC, are not assigned to any feed loading.

2.4 Ammonium Adsorption Experiments

An ammonium stock was prepared by dissolving 1 g ammonium chloride in 1 L deionized water. Working standards labeled 1, 2, 3, 4, and 5 mg L^{-1} were reacted with 0.2 mL Nessler reagent and measured at 450 nm. Absorbances were read on a Shimadzu UV-1280 spectrophotometer. The color-development time before reading, the final made-up volume, and the reagent blank were not recorded, and this is the only calibration: no

© 2026 The Authors | CC-BY 4.0

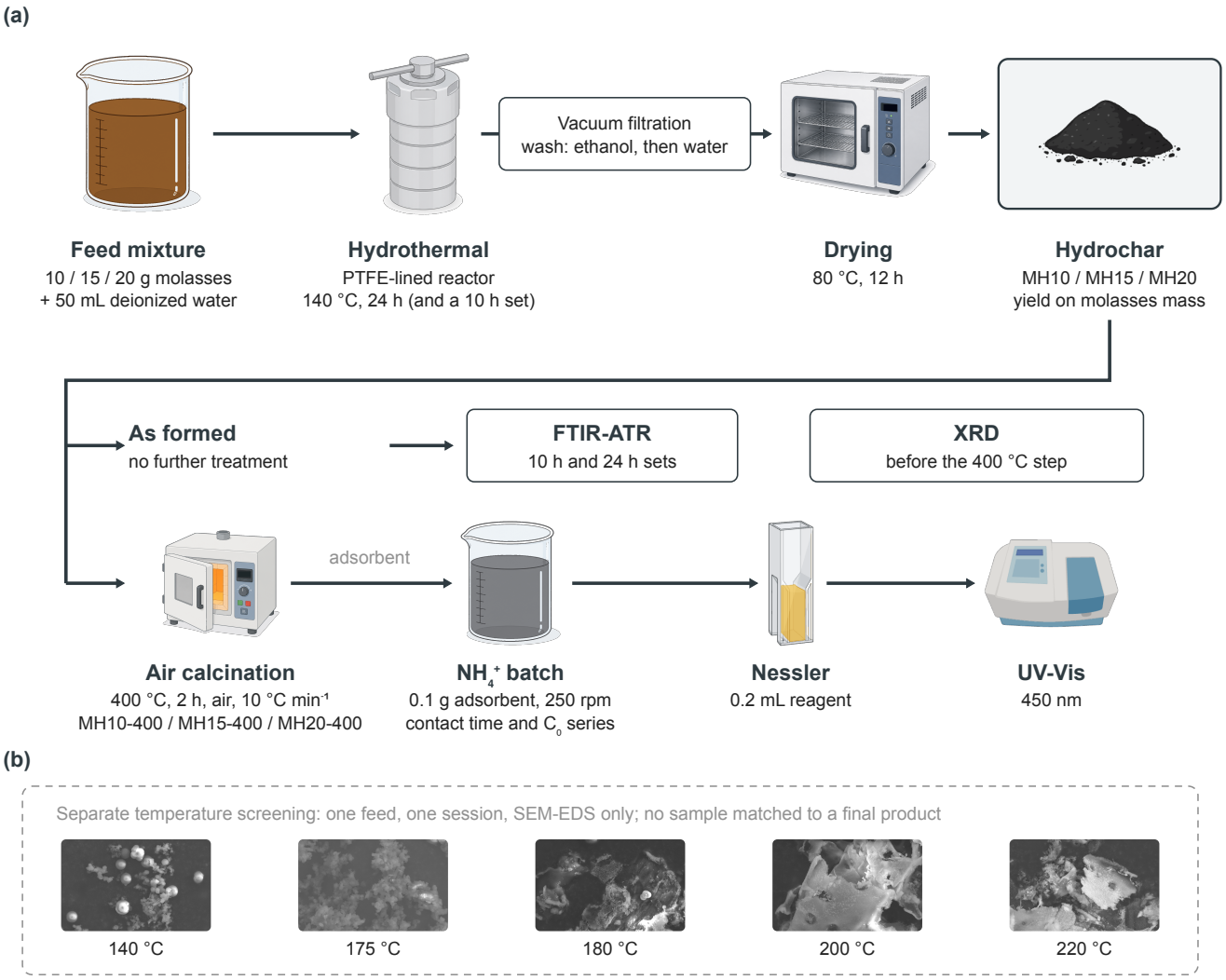

Figure 1. Preparation route and what each product was measured with. (a) Loading series; the 400 °C step separates the characterized hydrochar from the adsorbent. (b) Temperature screening, not matched to the loading series.

second curve reaches the absorbances at which the samples were read. Concentrations are expressed as NH_4^+ throughout.

Contact-time experiments used 0.1 g of MH10-400, MH15-400, or MH20-400 in 500 mL of a nominal 20 mg L^{-1} ammonium solution at 250 rpm. Contact times were 5, 10, 15, 30, 45, 60, 75, 90, 120, 150, and 180 min. Initial-concentration experiments used 0.1 g adsorbent in 100 mL solution at nominal concentrations of 5, 10, 20, 30, 40, 50, and 80 mg L^{-1} for 60 min at 250 rpm. Each condition was measured twice. A 10 mL aliquot was passed through a PTFE syringe filter, reacted with 0.2 mL Nessler reagent, and analyzed by UV-Vis spectroscopy. Solutions were neither pH-adjusted nor thermostatted, and pH and temperature were not measured; whether each time point came from an independent vessel or was drawn sequentially from one was not recorded. Sequential sampling would reduce the solution volume across the series, which Eq. (2) treats as constant.

Nominal adsorption capacity was calculated as

$$q_t = \frac{(C_0 - C_t)V}{m}, \tag{2}$$

where C_0 and C_t are the initial and remaining concentrations, V is the solution volume, and m is the adsorbent mass. They are termed nominal because most of the absorbances lie outside the calibration range.

2.5 Data Analysis

Every recorded 24 h synthesis batch was included in the yield analysis. Loading was related to wet-feed yield using Spearman's rank correlation [38] and compared among groups using the Kruskal–Wallis test [39]. Group sizes and production dates were unequal and were not adjusted for.

The five calibration standards were refitted by ordinary least squares. Contact-time observations were fitted directly, without linearization, to pseudo-first-order and pseudo-second-order models [40] and to a constant response after the first 5 min measurement, and the fits were compared by the small-sample corrected Akaike information criterion (AICc) [41, 42]. Langmuir [43], Freundlich [44], and linear partition models were fitted to the concentration series to test whether the observed concentration range bounds a saturation capacity; a Langmuir q_{max} that is not bounded by the data identifies no capacity, and such parameters are not interpreted. Two explanations for the out-of-range absorbances were tested against the constraint $C_e \leq C_0$: an undocumented dilution factor D, which scales every recovered concentration so that the largest admissible D is the minimum of C_0/C_e over each series, and a mismatch between the concentration basis of the standards and that of the stock, which enters as the same kind of constant and was evaluated for all six ordered pairs of NH_4Cl, NH_4^+, and ammonium nitrogen.

3. RESULTS AND DISCUSSION

3.1 Feed Loading and Hydrochar Recovery

The complete 24 h record contains five batches at 10 g, four at 15 g, and three at 20 g (Fig. 2 and Table 1). Mean wet-feed yield increased by 5.75 percentage points between 10 and 15 g, but by only 0.89 percentage points between 15 and 20 g. Feed loading was strongly

© 2026 The Authors | CC-BY 4.0

Table 1. Hydrochar recovery from all recorded 140 °C, 24 h batches. Yield is relative to the as-received molasses feed.

Molasses feed (g per 50 mL)	n	Yield (%)	Range (%)
10	5	11.74 ± 1.10	10.33–12.68
15	4	17.49 ± 1.30	16.49–19.24
20	3	18.38 ± 2.03	17.09–20.72

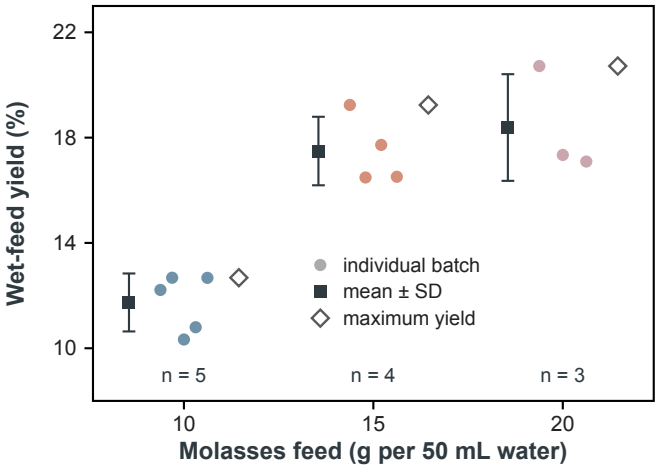

Figure 2. Hydrochar recovery from every recorded 140 °C, 24 h batch. Filled circles, individual batches, spread horizontally within each loading; square and bar, mean ± standard deviation (SD); open diamond, the maximum yield at that loading.

associated with yield ($\rho = 0.834$, $p = 0.00074$), and the three groups differed in the rank-based omnibus test ($p = 0.016$).

The maximum yield at each loading is 12.68, 19.24, and 20.72 %; reporting those three values alone would preserve the apparent direction of the response but suppress its spread. The full record supports an association between loading and recovered mass, not a clean causal loading effect: synthesis dates and group sizes are unbalanced, and the production sequence was neither randomized nor blocked. The small change from 15 to 20 g may indicate diminishing recovery at the highest solid-to-water ratio, but a balanced batch series is needed to test that interpretation.

Feed load is one of the variables through which hydrothermal carbonization distributes mass between the solid, liquid, and gas products [45], and for saccharides the concentration of the starting solution changes the particles themselves as well as how much of them is recovered [46]. These recoveries are not directly comparable with published yields, for two reasons that both work in the same direction: they are referred to the as-received molasses rather than to its dry matter, and 140 °C lies below the 170–240 °C range over which saccharide hydrochars are usually prepared [46].

3.2 Bulk Structural Similarity Across the Loading Series

All six spectra carry the same band set (Fig. 3a,b). Second derivatives resolve bands near 1700, 1610, 1510, 1455, 1315, 1210, and 1025 cm^{-1}, together with weaker features near 790 and 520 cm^{-1} and an aliphatic C–H band near 2920 cm^{-1}. Positions are reported to the nearest 5 cm^{-1} because the sampling interval is 5.737 cm^{-1}. Not every band clears the detection threshold in every spectrum, but the blanks track derivative noise, which differs fourfold across the six measurements, rather than composition. The 1700 cm^{-1} band is the most informative of the set for a sugar-derived char, and it is present in all six.

Above these, a broad envelope spans roughly 3000–3600 cm^{-1}. Its apparent maximum moves between 3310 and 3385 cm^{-1} across the six spectra as the smoothing window is varied, a range wider than any difference between samples, so a single position for it would describe the filter rather than the material, and none is quoted. Taken together the positions are consistent with a hydroxyl-rich, oxygen-containing carbon surface carrying carbonyl and C–O functionality, but the spectra do not resolve individual ester, ketone, ether, and carboxyl contributions without calibrated band fitting or supporting surface analysis.

Pairwise correlation of the absorbance spectra does not discriminate between these samples. Within the 24 h series it reaches $r = 0.990$–0.998, but the same statistic reaches 0.951–0.993 between the 24 h and 10 h series, which are different syntheses, and the strongest cross-series pair scores above two of the three within-series pairs. Two carbons sharing any absorbance envelope correlate at that level; the similarity above rests on the band set.

XRD patterns are similarly close ($r = 0.997$–0.998; Fig. 3c) and are dominated by broad scattering. Broad diffraction is expected for sugar-derived secondary char, which commonly forms amorphous carbon spheres [5]. These patterns support predominantly amorphous products with comparable bulk fingerprints. They do not support precise crystallinity values: the 8.58–9.79 % crystallinity figures cannot be checked, since the baseline, integration limits, and peak decomposition behind them were not recorded.

The apparent position of the amorphous maximum is not, however, a safe summary statistic here. Smoothing the raw patterns places the maximum near 21.39, 20.99, and 24.95° 2θ for MH10, MH15, and MH20. The outlying value for MH20 is not a property of the carbon: it is a narrow reflection at 25.4° superimposed on the envelope. Excluding 24.6–26.2° and repeating the identical smoothing moves that maximum to 21.34°, while the 10 and 15 g values are unchanged to two decimals. All three hydrochars share an amorphous maximum at 21.0–21.4°, and the bulk similarity is closer than the raw positions suggest.

That envelope should not be read as a graphitic stacking reflection. Fitting the corrected band gives an interlayer spacing of 4.01–4.08 Å, against 3.354 Å for graphite and the 3.44 Å spacing of fully turbostratic carbon [47]; the Mering–Maire graphitization degree [48] evaluates to −6.6 to −7.4, far outside its physical range of 0 to 1, which places the material outside the domain of the expression rather than at its disordered end. The apparent stack height of 0.75–0.78 nm corresponds to 1.9 layers, and a stack of fewer than two layers is not a stack, so the fit contradicts the assignment it would rest on. No (10) band is present near 43° ($S/N = 1.3$–2.1), leaving the lateral dimension of any aromatic domains unmeasured.

All three observations are consistent with carbonization at 140 °C yielding a humin-like polymeric solid from sugar dehydration and condensation [5] rather than a turbostratic carbon. Establishing a degree of carbonization would require elemental H/C and O/C ratios, Raman I_D/I_G [49], or proximate fixed carbon, none of which was measured for these batches. The 8.58–9.79 % figures quoted above are crystalline-area fractions and are not a carbonization measure. The only crystalline phase detected anywhere in this series is anhydrite, and it is present in one of the three products, so those fractions cannot be read as the ordered part of a carbon phase in any of them.

The structural result narrows the interpretation of Section 3.1. Increasing the molasses feed recovered more dry solid, particularly between 10 and 15 g, without producing a comparably large change in the FTIR or XRD fingerprint. Surface area, elemental composition, acidity, and cation-exchange capacity were not measured, so bulk similarity cannot be extended to the adsorption sites.

3.3 Residence Time Separates the Oxygen-Band Ratios

The three 10 h spectra were acquired in the same session as the 24 h set and share its band positions, so the two residence times can be compared directly. Because attenuated-total-reflection absorbance scales with contact pressure, the comparison is made on ratios to the 1610 cm^{-1} band rather than on absolute heights (Fig. 3b and Table 2).

© 2026 The Authors | CC-BY 4.0

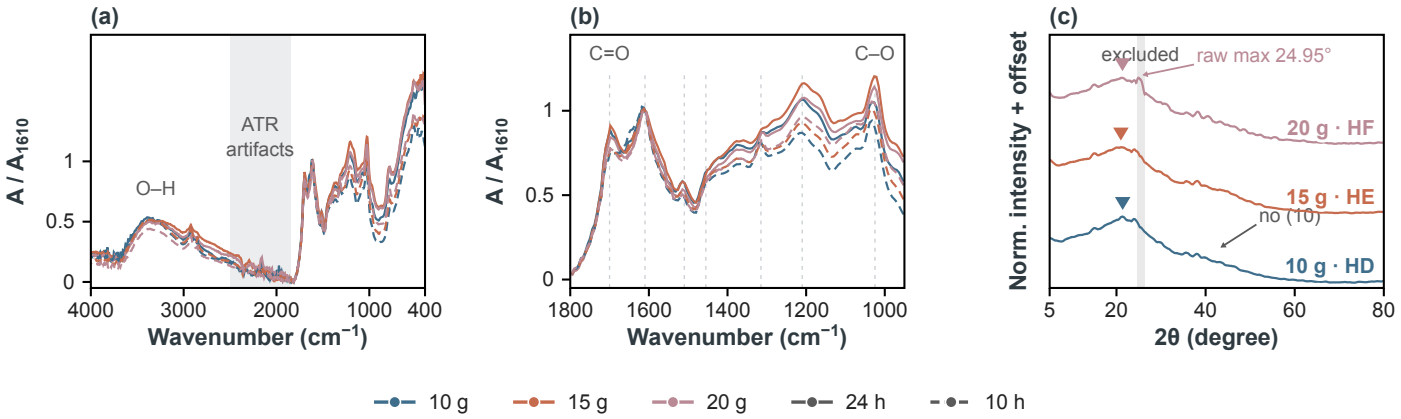

Figure 3. Bulk structure of the provisionally mapped hydrochars. (a) The six FTIR spectra, each divided by its own 1610 cm^{-1} band; color, feed loading; dashing, the 10 h series; shading, the excluded diamond-phonon and CO_2 interval. (b) The 950–1800 cm^{-1} region, with guides at the resolved band centers. (c) XRD patterns of the three 24 h products, normalized and offset; gray band, the 24.6–26.2° interval excluded before the envelope maximum was located; triangles, the masked maxima; annotation, the raw 20 g maximum.

Table 2. Infrared band ratios against the 1610 cm^{-1} band, by residence time. Each series holds one spectrum from each feed loading, so the spread within a series contains the loading variation as well as measurement variation.

Band (cm^{-1})	10 h (n = 3)	24 h (n = 3)	Ranges
1700 (C=O)	0.755 ± 0.013	0.861 ± 0.032	separate
1025 (C–O)	0.984 ± 0.068	1.131 ± 0.077	separate
1510	0.501 ± 0.012	0.561 ± 0.027	separate
1315	0.811 ± 0.006	0.872 ± 0.013	separate
3350 (O–H)	0.489 ± 0.046	0.510 ± 0.015	overlap

Four of the five ratios have non-overlapping ranges between the two residence times, and all four move in the same direction: the 24 h products are richer in carbonyl and C–O absorbance relative to the 1610 cm^{-1} band. Saccharides carbonize hydrothermally through dehydration, condensation, and aromatization into microspheres whose hydroxyl, carbonyl, and carboxyl groups sit in a shell around a more aromatic core [46, 50], and attenuated total reflection samples that shell rather than the particle interior. The separation is the only measurable difference between synthesis conditions anywhere in this dataset. Its direction is not, however, the one a more severe treatment would give: raising temperature or residence time in hydrothermal carbonization lowers the oxygen content of the solid [51], which on the usual band assignments would lower these ratios rather than raise them.

It is a lead rather than a result. Each series contains one spectrum per feed loading and no replicate measurement, so loading variation and residence-time variation are not separated, and the width of each range is not an uncertainty on a mean. A replicated set at both residence times, with elemental analysis to anchor the band ratios to H/C and O/C, would settle whether the separation survives.

3.4 Crystalline Calcium Phases Differ Between Batches

The 25.4° reflection that displaces the apparent maximum of the 20 g pattern is the strongest line of anhydrite, $CaSO_4$. Seven of its eight reference lines above 10 % relative intensity are present in the 20 g pattern, and all eight in HB and HC. Two of those eight lie 0.06° apart and are not resolved separately, so the intensities compare over seven lines: 100:29:21:25:12:11:14 for HB and 100:22:23:20:15:10:9 for HC, against 100:29:20:20:16:15:11 for the card. Two of the unassigned patterns carry a second phase, weddellite ($CaC_2O_4 \cdot 2H_2O$) [52], identified from its 14.32° and 32.23° lines. Fig. 4a shows the six patterns against both reference stick patterns, and Table 3 summarizes the assignments.

The two hydrochars assigned to MH10 and MH15 contain no crystalline phase above a five-sigma detection limit [53] of 222 counts × degree of integrated line area; MH20 sits 1.8 times above that limit. Gypsum, bassanite, sylvite, and halite were tested and rejected, as were the two negative controls: whewellite fails because none of its 100, 70, 45, and 30 % lines appear in any pattern, which is what separates the oxalate dihydrate from the monohydrate, and calcite fails because its 100 % line is absent throughout. Fig. 4b shows the line itself in the three patterns mapped to final products. The feature near 24.3° in that panel is not a second reflection: it is the residual shoulder of the amorphous envelope, common to all three at similar amplitude and outside the integration window.

Infrared spectroscopy does not corroborate the assignment. The sulfate ν_4 region, 580–690 cm^{-1}, resolves no band in any of the three 24 h spectra, and its integrated absorbance is the same within noise for all three (S/N = 1.7–1.9), with the MH20 not the largest. A few weight percent of a mineral inside a dominant organic matrix, sampled through a single-reflection diamond crystal, lies below what this measurement resolves, so the absent band does not bear on the diffraction result.

Energy-dispersive spectroscopy would test calcium and sulfur directly, and six such analyses were run, but they cannot settle this question for two independent reasons. They were run on the temperature screening rather than on the feed-loading series, so none of them is MH20; and the quantification model was fixed at carbon, oxygen, sodium, silicon, iron, and nickel, with calcium and sulfur absent from it (Section 3.5). A repeat on the three final products, with calcium and sulfur declared and the raw spectra retained, would settle it.

Calcium, sulfate, and oxalate are all constituents of cane molasses, which carries some 13.1 % ash on a dry basis, with calcium at 1.39 % and sulfate at 2.09 % of dry matter [1]. The simplest reading is therefore that feed ash components precipitate during carbonization rather than that a carbon phase crystallizes. Ash-forming elements are known to partition between the solid product and the process water during hydrothermal carbonization rather than to remain with the feed as a whole [54, 55], so the calcium carried into the solid may differ from batch to batch. The anhydrous rather than hydrated form is not a preparation artifact: the diffraction specimens were taken before the 400 °C treatment, which would itself have dehydrated any gypsum through bassanite to anhydrite [56]. These patterns therefore describe the product as formed rather than the adsorbent, which passed through that step; since the step produces anhydrite rather than removing it, the difference between batches is expected to persist into the adsorbent, though the adsorbent was not itself examined by diffraction. What the difference tracks is still open, since HA, HB,

© 2026 The Authors | CC-BY 4.0

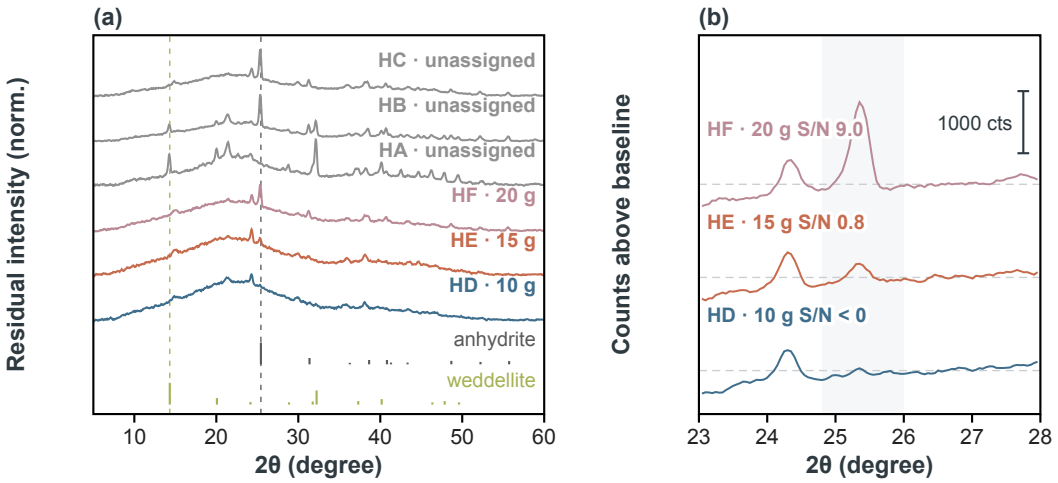

Figure 4. Crystalline phases in the diffraction patterns. (a) The six patterns after subtraction of the amorphous background, normalized and offset; sticks, PDF-2 reference lines above 10 % relative intensity for anhydrite ($CaSO_4$, 37-1496) and weddellite ($CaC_2O_4 \cdot 2\,H_2O$, 17-0541); dashed guides, 25.44° and 14.32°; gray, the patterns not assigned to a feed loading. (b) The anhydrite 25.4° line in the three assigned products, on a linear baseline from the 23.6–24.6° and 26.2–27.2° shoulders; shading, the integration window; signal-to-noise ratios as in Table 3.

Table 3. Crystalline phases detected in the diffraction patterns. Detection is by matched reference lines above 10 % relative intensity. The last column is the signal-to-noise ratio of the integrated anhydrite 25.4° line.

Pattern	Assigned feed	Phase	Lines matched	Anhydrite S/N
HA	unassigned	weddellite	6/9	< 0
HB	unassigned	weddellite, anhydrite	4/9, 8/8	42.3
HC	unassigned	anhydrite	8/8	13.1
HD	10 g	none detected	–	< 0
HE	15 g	none detected	–	0.8
HF	20 g	anhydrite	7/8	9.0

and HC are unassigned and feed loading, production batch, and washing therefore cannot be separated. What the data do establish is that the three patterns mapped to final products are not equivalent in mineral content, even though their carbon envelopes coincide. An adsorption comparison across these loadings would therefore not be comparing carbon surfaces alone.

3.5 A Separate Temperature Screening

The electron microscopy is not part of the loading series. It covers five carbonization temperatures at a single feed, was acquired in one session before the first recorded 24 h batch, and carries one spectrometer report per temperature plus one repeat. None of its samples can be matched to a final product, but it accounts for the choice of 140 °C and its compositions qualify Section 3.4.

Morphology changes across the series (Fig. 5a–e). At 140 °C the field contains discrete carbonaceous microspheres dispersed among smaller irregular aggregates, the form commonly reported for sugar-derived secondary char [5]. From 175 °C upward no discrete spheres remain: the product appears as fused sheet and block material with rough surfaces. Each temperature is represented by one field, so this is a qualitative contrast rather than a measured transition, but it is consistent with the choice of 140 °C for the loading series, the temperature that yields separable particles.

Nine diameter lines recorded on a 10000× micrograph give (2.42 ± 1.11) µm, with a range of 1.03–4.04 µm, inside the 0.4–6 µm range reported for saccharide hydrochar spheres [46]. Only the magnification was recorded with those lines, and five samples were imaged at that magnification, so the measurement record alone does not fix which field they were drawn on. Searching each candidate micrograph for a line reproducing the recorded length, angle, and gray statistics does not settle it either: with about 1.4 million placements available per line, coincidental matches are common. Only the 175 °C field is excluded outright, on gray range. The strongest argument remains the morphology, since diameters of this kind can only be drawn where discrete spheres exist.

The spectra themselves carry a line the reports do not (Fig. 5f and Table 4). A peak at 3.69 keV, calcium Kα, is present at 180, 200, and 220 °C at six times the local scatter and absent at 140 °C. The assignment survives its controls: potassium Kα, whose line is the nearest competitor, is absent everywhere; calcium Kβ is absent as expected at roughly a tenth of Kα; a blank window at 5.5 keV returns nothing; and the 10 kV beam over-volts calcium Kα by a factor of 2.7, so a missing line would not be an excitation artifact. The 220 °C analysis was repeated five days later and reproduces both the composition, to 0.4 % in O/C, and the calcium line.

Calcium was never in the quantification model. Because the printed masses are normalized over the six declared elements, its counts are not merely unreported but redistributed among them, so the carbon and oxygen percentages for the three calcium-bearing samples are wrong rather than incomplete. The O/C column measures the size of that displacement and is not a carbonization index: it is also non-monotonic, rests on one measurement per temperature at varying working distance, and carries printed relative errors of 14 % on carbon and 19–22 % on oxygen. Sulfur was not detected in any spectrum.

Two consequences follow. The 140 °C product of this screening carries no detectable calcium, which is the same direction as the diffraction result for MH10 and MH15, though on a different sample. And interpreting the three final products requires an elemental analysis with calcium and sulfur declared from the start.

3.6 Analytical Range Limits the Adsorption Claims

The calibration standards form a linear relation within 1–5 mg L^{-1}, $A = 0.0319C + 0.0119$ ($R^2 = 0.999892$; Fig. 6a). The high R^2 describes those five standards only, and they span absorbances of 0.044 to 0.171. A coefficient of determination is in any case not a test of linearity: calibration curves with the larger R^2 can fail an objective polynomial test that curves with the smaller R^2 pass, so a linear range has to be measured rather than read off a fit [57, 58]. The samples span 0.114 to 0.777, so the calibration characterizes 22 % of the absorbance range in which the

© 2026 The Authors | CC-BY 4.0

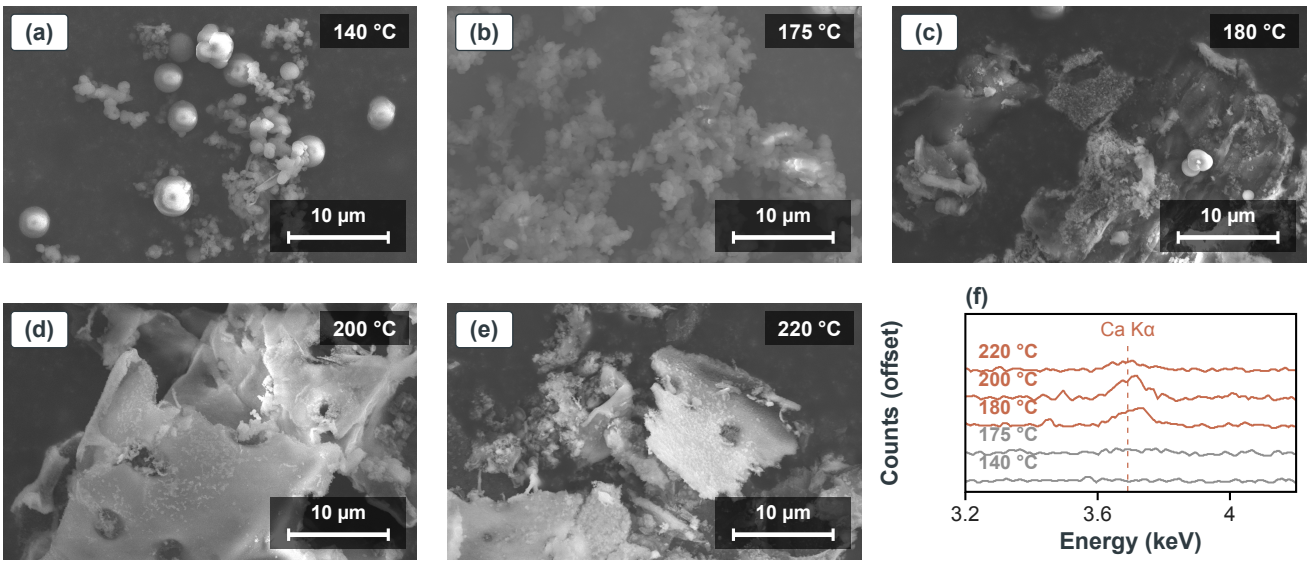

Figure 5. The temperature screening. (a–e) Secondary-electron micrographs at 10000× of hydrochars labeled 140, 175, 180, 200, and 220 °C; discrete microspheres appear only in the 140 °C field. (f) Energy-dispersive spectra over the calcium Kα region, offset vertically; traces in color exceed five times the local scatter at 3.691 keV, those in gray do not. Traces were digitized from the instrument plots and indicate the presence or absence of a line, not a concentration.

Table 4. Elemental composition printed in the spectrometer reports, with the calcium the quantification model omitted. Mass percentages are normalized over the six declared elements. The last column is the calcium Kα excess measured on the digitized spectra, in units of the local scatter.

Sample	C (%)	O (%)	Minor (%)	O/C at.	Ca Kα
140 °C	74.18	25.33	0.50	0.256	0.3σ
175 °C	74.92	24.74	0.34	0.248	2.2σ
180 °C	69.18	30.77	0.05	0.334	**6.6**σ
200 °C	65.33	33.85	0.81	0.389	**6.4**σ
220 °C	73.16	26.52	0.32	0.272	**6.4**σ
220 °C repeat	73.41	26.48	0.10	0.271	**5.3**σ

measurements were made. All 66 contact-time samples and 36 of the 42 concentration-series samples lie above the top standard; the largest inferred C_e is 23.98 mg L^{-1}, 4.80 times the upper standard. The stock solutions were never read against this curve either, since no recorded absorbance approaches the value that any of the seven nominal C_0 would require: the highest reading anywhere is 0.777, against the 2.564 implied by 80 mg L^{-1}. Every removal percentage is therefore referred to an assumed rather than a measured initial concentration, and absolute C_e, removal, and q are unvalidated outside the shaded interval in Fig. 6a.

Two explanations would restore these values without new measurements, and neither is consistent with the measurements themselves. Had the samples been diluted before reading and the factor lost, the true C_e would be D times the reported one; because adsorption requires $C_e \leq C_0$, the largest admissible D is 1.18, whereas the smallest dilution in routine laboratory use, twofold, already implies C_e/C_0 as high as 1.69. A lost dilution would in any case displace the values in the wrong direction, making the reported concentrations too low where they are already too high for their calibration. The standards and the stock might instead be expressed on different bases, as NH_4^+, as ammonium nitrogen, or as NH_4Cl, which enters as the same kind of constant factor; three of those six ordered pairs satisfy $C_e \leq C_0$, but a change of basis rescales the concentration axis without moving a single absorbance, so relabeling leaves the range problem untouched.

The exposure is narrower than a general loss of validity. Every sample absorbance lies below 1.0, where a photometer is ordinarily still linear, so detector saturation is an unlikely source of error. The assumption the extrapolation carries is chemical rather than optical. Nessler determinations have been verified against nominal concentration up to about 8 mg L^{-1} [59], several times below the largest value inferred here, so the extrapolation runs past the range over which the chemistry itself has been checked. Color development also depends on the reaction time, for which 10 to 30 min is recommended [59] and which was not recorded. Reagent depletion and incipient turbidity would each bias the reading low, which would inflate the apparent removal rather than scatter it. Both are documented for this chemistry: the color-forming reaction consumes reagent in proportion to the ammonia present, so an incomplete reaction underestimates the concentration, and hardness cations precipitate as hydroxides in the strongly alkaline reagent unless a complexing agent is added, producing turbidity [60]. Calcium is present in these products (Section 3.4), although whether any of it entered solution was not measured. These data cannot test either mechanism; a standard series covering the absorbance range the samples themselves occupy would settle it directly.

A validated concentration would still not assign the removal to the carbon surface. The adsorbent had been heated to 400 °C in air, which oxidizes part of the hydrochar carbon and concentrates its ash in the residue [31, 61], and the calcium phase of Section 3.4 passes through that step as anhydrite. Ammonium could therefore leave solution by cation exchange against alkali and alkaline-earth cations released from the ash, by electrostatic attraction to deprotonated oxygen groups, or by complexation at those groups [24, 25]. Its apparent removal could also arise without uptake, if released calcium made the Nessler solution turbid or if alkaline ash raised the pH toward the NH_4^+/NH_3 pK_a of 9.25, where agitation favors loss of NH_3 [62, 63]. Solution pH and dissolved cations were measured neither before nor after contact, so none of these pathways can be excluded.

The shape of the time series adds a separate constraint (Fig. 6b). Correlations between the two replicate curves are 0.11, −0.03, and −0.39 for MH10-400, MH15-400, and MH20-400, respectively, while mean absolute replicate differences in nominal q_t are 5.56–5.92 mg g^{-1} (Table S1). Nominal q_t peaks at 15, 120, and 75 min, the absorbance minima in Fig. 6b; after the first reading the values fluctuate rather than approach

© 2026 The Authors | CC-BY 4.0

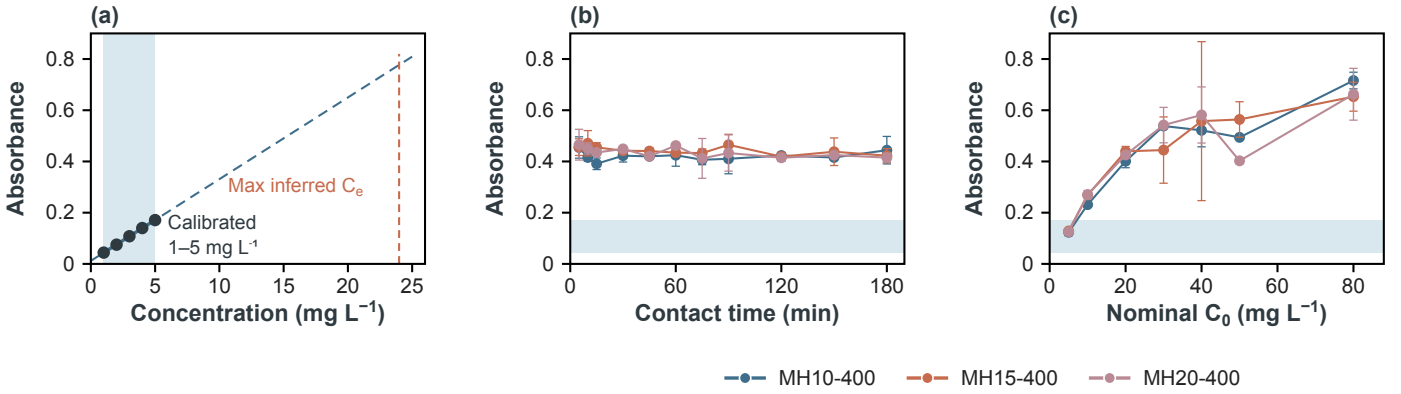

Figure 6. Analytical constraint on the ammonium dataset. (a) Calibration standards and extrapolated line; shading, calibrated interval; dashed line, maximum inferred equilibrium concentration. (b) Contact-time and (c) initial-concentration series as measured absorbance at 450 nm; shading, absorbance range of the standards. Points and bars, duplicate means ± SD. Nominal values derived from these absorbances are listed in Tables S1 and S2.

Table 5. Hydrothermal carbons from molasses, sugars, and sugar-industry residues compared with the present hydrochars. Capacities in mg g^{-1} as reported; –, not reported; MB = methylene blue; RhB = rhodamine B.

Feedstock and HTC conditions	Yield (%)	S_{BET} (m^2 g^{-1})	FTIR groups	Adsorbate: capacity	Regeneration	Limitation	Ref.
Cane molasses (this study), 140 °C, 24 h, 10–20 g per 50 mL	11.7–18.4[a]	not measured	O–H, C=O, C=C, C–O	NH_4^+: not validated[b]	–	treated adsorbent not characterized	
Date-palm molasses, 180–250 °C, 2–10 h, 4 g per 25 mL	≤40.4	<1	O–H, C=O, C=C, C–O	MB: 12	–	single capacity value	[10]
Date molasses, HTC then H_3PO_4 activation	–	1584	–	MB: 410	–	porosity from chemical activation	[11]
Wood chips and cane molasses, K_2FeO_4-assisted HTC	–	–	O-groups, Fe–O	tetracycline: 119.7 (unmodified 56.4)	–	iron-modified composite	[12]
Sucrose, 200 °C, 12 h, 15 g per 200 mL	26.7	1.60	O–H, C=O, C=C, C–O	MB: 2.07; RhB: 3.51	10 cycles	linearized Langmuir fit	[28]
Sugarcane bagasse, 250 °C, 0.5–3 h, 1:5	–	1.4–1.8	C=O, C=C, C–O–C	NH_4^+: 2.97–3.43 (pH 7)	–	linearized Langmuir fit	[21]
Sugarcane leaf, 200–240 °C	–	–	–	NH_4^+: 20 (synthetic), 10.25 (digestate)	–	competition by Mg^{2+} and K^+	[22]
Paper sludge, 200 °C, 24 h, 0.25 M NaOH	–	2.2	O–H, C=O	NH_4^+: 20.09	≈50 % after 5 cycles	low porosity	[23]
Bagasse and vinasse with H_3PO_4, 230 °C, 13 h	–	11.92	O–H	atrazine: 0.273; fipronil: 0.035	–	low affinity	[15]
Bagasse and vinasse HTC, then KOH at 500–700 °C	–	870	fewer acidic and phenolic groups	fipronil: 249	–	activated carbon rather than hydrochar	[16]

[a] Wet-feed basis; other yields on the basis each study defines. [b] Measurements above the 1–5 mg L^{-1} calibration (Section 3.6).

three resolved plateaus. Nonlinear pseudo-first-order, pseudo-second-order, and constant-after-5 min descriptions all lie within $\Delta AICc \leq 2.1$. The data cannot distinguish these models, and a pseudo-second-order fit cannot be used to assign chemisorption: the apparent generality of that rate law has been traced to modeling conventions that favor it rather than to the systems it is fitted to [27].

Absorbance after 60 min rises with nominal initial concentration in all three series (Fig. 6c), and so does nominal q_{60} (Table S2), but none reaches a plateau. None of the three series bounds a Langmuir capacity: direct nonlinear fits drive q_{max} toward approximately 1×10^6 mg g^{-1} while K_L approaches zero, which is the Langmuir form collapsing onto a straight line through the observed 5–80 mg L^{-1} range. Neither parameter carries physical meaning here. A linearized fit would have concealed the same failure behind a finite q_{max} and a high R^2 [26]. Freundlich is not consistently preferred over a linear partition model among the three samples [64]. More importantly, an equilibrium isotherm requires both validated concentrations and a separately established equilibrium time. Neither requirement is met here.

The adsorption experiment therefore remains preliminary. Its safest qualitative observation is that nominal removal had occurred before the first 5 min reading and that nominal mass uptake increased with initial concentration. Reporting an optimum time, kinetic mechanism, isotherm family, or maximum capacity would assign more information to the data than they contain.

3.7 Comparison with Reported Sugar-Derived Hydrochars

Table 5 places the present products beside recent hydrothermal carbons from molasses, sugars, and sugar-industry residues. Unactivated hydrochars prepared at 180 to 250 °C were nearly non-porous: BET areas were below 1 m^2 g^{-1} for date-palm molasses [10], 1.60 m^2 g^{-1} for sucrose [28], 1.4 to 1.8 m^2 g^{-1} for bagasse [21], and 2.2 m^2 g^{-1} for paper sludge [23], within the 1.0 to 3.5 m^2 g^{-1} reported for glucose hydrochars [65]. Areas of 870 to 1584 m^2 g^{-1} and capacities above 240 mg g^{-1} appeared only after phosphoric acid or KOH activation [11, 16], which converts the hydrochar into an activated carbon. Ammonium capacities of the unmodified hydrochars lay between about 3 and 20 mg g^{-1} [21–23], a range narrow enough that an analytical error of the size shown in Section 3.6 would change the ranking of these materials. Regeneration was reported for two of the nine studies [23, 28]. The present products extend the comparison to 140 °C, below the temperature of any study in Table 5, with yield recorded for every batch; their surface area was not measured, and their ammonium data cannot be placed beside the capacities listed.

3.8 Experimental Requirements for a Defensible Adsorption Comparison

The loading series can be tested without changing its central design. Each final hydrochar should first be linked to an independently labeled synthesis batch. The ammonium calibration must include a reagent blank, replicated standards, and standards spanning the absorbance range the samples themselves occupy rather than the nominal concentration range alone, with the upper limit of the linear range established by an objec-

© 2026 The Authors | CC-BY 4.0

tive test rather than inferred from a coefficient of determination [57] and with the standards made up in a matrix that matches the samples [60]. The stock solutions should be read against that curve rather than assumed. Samples still exceeding it should be diluted and the factors retained, with the reagent verified to remain in excess at the top of the range. Independent vessels at each time point would avoid the changing-volume problem of sequential sampling, and time points before 5 min are needed to resolve the initial uptake. An adsorbent-free ammonium control and an ammonium-free adsorbent blank would separate uptake from losses in solution and from interference by species released from the solid. Solution pH should be controlled, recorded before and after contact, and varied across the range where NH_4^+ converts to NH_3, and dissolved calcium and potassium measured before and after contact would test exchange against the ash cations. Removal percentage and q_e should be reported together, with the dose, volume, and measured C_0, because removal alone scales with the dose.

An equilibrium time should be established before collecting an isotherm, and the concentration range should extend far enough to test whether saturation is present. Surface area and pore-size distribution [66], elemental composition, and pH-dependent surface charge [67] or cation-exchange capacity are required before the comparable FTIR/XRD patterns can be related to ammonium affinity, and they have to be measured on the treated adsorbent itself rather than on the hydrochar it came from. Together these measurements would allow a direct comparison of material performance across the loading series.

4. CONCLUSIONS

Hydrothermal carbonization at 140 °C converted cane molasses directly to a solid, and we compared product recovery, bulk structure, and an ammonium dataset across three feed loadings. Mean wet-feed yield rose from 11.74 % at 10 g to 17.49 % at 15 g per 50 mL water, whereas the three products kept closely matching FTIR and XRD fingerprints ($r = 0.997$–0.998). The highest mean yield, 18.38 % at 20 g, exceeded the 15 g value by less than one standard deviation, and only that product carried anhydrite. The series therefore differs in mineral content rather than in carbon structure, consistent with feed-ash calcium and sulfate precipitating during carbonization. The ammonium measurements lay above a 1–5 mg L^{-1} calibration in all 66 contact-time and 36 of 42 concentration-series samples, so they establish no capacity, kinetic model, or isotherm. For molasses valorization, feed loading sets how much solid is recovered, whereas the ash carried with the feed decides whether two batches are the same material; a calibration-range test is a precondition for ranking such products by adsorption. The next step is an ammonium series within a validated Nessler range, with measured C_0, blanks, controlled pH, and characterization of the 400 °C-treated adsorbent itself.

SUPPLEMENTARY MATERIAL

Supplementary Information: Table S1, contact-time series; Table S2, initial-concentration series; nominal values derived from the measured absorbances (PDF).

CRediT AUTHORSHIP CONTRIBUTION STATEMENT

Sephia Amanda Muhtar: Investigation, Data curation, Writing – original draft. **Kamilah Nada Maisa:** Writing – review & editing. **Kholik Hidayatullah:** Writing – review & editing. **Abdul Latief Salim Azpar:** Writing – review & editing. **Alam Hannaan Muhammad:** Writing – review & editing. **Panji Setyo Nugroho:** Writing – review & editing. **Andika Munandar:** Conceptualization, Methodology, Formal analysis, Supervision, Writing – review & editing.

DECLARATION OF COMPETING INTEREST

The authors declare no competing financial interests.

DATA AVAILABILITY

The raw dataset, the analysis scripts, and the derived tables will be made available on request.

FUNDING

This research received no external funding.

REFERENCES

[1] A. Palmonari, D. Cavallini, C. Sniffen, L. Fernandes, P. Holder, L. Fagioli, I. Fusaro, G. Biagi, A. Formigoni, L. Mammi, Short communication: Characterization of molasses chemical composition, Journal of Dairy Science 103 (2020) 6244–6249. doi:10.3168/jds.2019-17644.

[2] S. Zhang, J. Wang, H. Jiang, Microbial production of value-added bioproducts and enzymes from molasses, a by-product of sugar industry, Food Chemistry 346 (2021) 128860. doi:10.1016/j.foodchem.2020.128860.

[3] J. Fito, N. Tefera, S. W. H. Van Hulle, Sugarcane biorefineries wastewater: bioremediation technologies for environmental sustainability, Chemical and Biological Technologies in Agriculture 6 (2019) 6. doi:10.1186/s40538-019-0144-5.

[4] X. Zhang, Y. Wang, J. Cai, K. Wilson, A. F. Lee, Bio/hydrochar sorbents for environmental remediation, Energy & Environmental Materials 3 (4) (2020) 453–468. doi:10.1002/eem2.12074.

[5] G. Ischia, M. Cutillo, G. Guella, N. Bazzanella, M. Cazzanelli, M. Orlandi, A. Miotello, L. Fiori, Hydrothermal carbonization of glucose: Secondary char properties, reaction pathways, and kinetics, Chemical Engineering Journal 449 (2022) 137827. doi:10.1016/j.cej.2022.137827.

[6] R.-J. van Putten, J. C. van der Waal, E. de Jong, C. B. Rasrendra, H. J. Heeres, J. G. de Vries, Hydroxymethylfurfural, a versatile platform chemical made from renewable resources, Chemical Reviews 113 (3) (2013) 1499–1597. doi:10.1021/cr300182k.

[7] H. S. Kambo, A. Dutta, A comparative review of biochar and hydrochar in terms of production, physico-chemical properties and applications, Renewable and Sustainable Energy Reviews 45 (2015) 359–378. doi:10.1016/j.rser.2015.01.050.

[8] A. Funke, F. Ziegler, Hydrothermal carbonization of biomass: A summary and discussion of chemical mechanisms for process engineering, Biofuels, Bioproducts and Biorefining 4 (2) (2010) 160–177. doi:10.1002/bbb.198.

[9] B. M. Ghanim, D. S. Pandey, W. Kwapinski, J. J. Leahy, Hydrothermal carbonisation of poultry litter: Effects of treatment temperature and residence time on yields and chemical properties of hydrochars, Bioresource Technology 216 (2016) 373–380. doi:10.1016/j.biortech.2016.05.087.

[10] M. El-Harbawi, S. Alhawtali, A. S. Al-Awadi, L. El Blidi, M. M. Alrashed, A. Alzobidi, C.-Y. Yin, Synthesis of carbon microspheres from inedible crystallized date palm molasses: Influence of temperature and reaction time, Materials 16 (4) (2023) 1672. doi:10.3390/ma16041672.

[11] S. Alhawtali, M. El-Harbawi, A. S. Al-Awadi, L. El Blidi, M. M. Alrashed, C.-Y. Yin, Enhanced adsorption of methylene blue using phosphoric acid-activated hydrothermal carbon microspheres synthesized from a variety of palm-based biowastes, Coatings 13 (7) (2023) 1287. doi:10.3390/coatings13071287.

[12] T. He, X. Zhou, Z. Bao, S. Fu, X. Lin, Preparation of hydrochar by one-step hydrothermal carbonization with potassium ferrate-assisted activation for the removal of tetracycline in water, Journal of Chemical Technology & Biotechnology 98 (8) (2023) 2039–2050. doi:10.1002/jctb.7417.

[13] N. Zhang, X. Jiang, D. Ren, Y. Liu, Y. Li, X. Zeng, Z. Huo, A magnetic amino enriched hydrothermal carbon production with molasses as carbon source, Journal of Environmental Chemical Engineering 10 (1) (2022) 107073. doi:10.1016/j.jece.2021.107073.

[14] S. Bhowmick, Y. Shastri, A. Garg, Hydrothermal pretreatment of press mud: Characterization and potential application of hydrochar and process water, Waste Management 183 (2024) 143–152. doi:10.1016/j.wasman.2024.05.004.

[15] A. T. B. de Carvalho, L. de Souza Leite, B. D. C. Vizioli, S. J. de Andrade, M. C. Bisinoti, C. C. Montagner, Application of sugar cane bagasse hydrochar for fipronil and atrazine removal from water, ACS Omega 10 (46) (2025) 55544–55553. doi:10.1021/acsomega.5c06438.

[16] G. A. Nogueira, M. J. Laranja, S. A. Mondek, L. H. S. Vieira, M. Boscolo, O. P. Ferreira, A. B. Moreira, M. C. Bisinoti, Tailoring koh-activated hydrochar derived from sugarcane industry by-products through an adsorption study with fipronil, ACS Sustainable Resource Management 2 (10) (2025) 1977–1985. doi:10.1021/acssusresmgt.5c00321.

[17] J. Huang, N. R. Kankanamge, C. W. K. Chow, D. T. Welsh, T. Li, P. R. Teasdale, Removing ammonium from water and wastewater using cost-effective adsorbents: A review, Journal of Environmental Sciences 63 (2018) 174–197. doi:10.1016/j.jes.2017.09.009.

[18] J. A. Camargo, Á. Alonso, Ecological and toxicological effects of inorganic nitrogen pollution in aquatic ecosystems: A global assessment, Environment International 32 (6) (2006) 831–849. doi:10.1016/j.envint.2006.05.002.

[19] N. Normah, N. Juleanti, N. R. Palapa, T. Taher, P. M. S. B. N. Sire-

© 2026 The Authors | CC-BY 4.0

gar, A. Wijaya, A. Lesbani, Hydrothermal carbonization of rambutan peel (Nephelium lappaceum L.) as a green and low-cost adsorbent for Fe(II) removal from aqueous solutions, Chemistry and Ecology 38 (3) (2022) 284–300. doi:10.1080/02757540.2022.2040996.

[20] C. A. Takaya, L. A. Fletcher, S. Singh, K. U. Anyikude, A. B. Ross, Phosphate and ammonium sorption capacity of biochar and hydrochar from different wastes, Chemosphere 145 (2016) 518–527. doi:10.1016/j.chemosphere.2015.11.052.

[21] P. A. Trazzi, M. Vashishtha, J. Najser, A. Schmalenberger, V. K. Kannuchamy, J. J. Leahy, W. Kwapinski, Adsorption of ammonium, nitrate, and phosphate on hydrochars and biochars, Applied Sciences 14 (6) (2024) 2280. doi:10.3390/app14062280.

[22] E. Kurniawan, R. Jariyaboon, A. Reungsang, P. Kongjan, Ammonium adsorption from anaerobic digestate on sugarcane hydrochar: performance, competitive ion mechanisms, and biorefinery integration, Environmental Science and Pollution Research 33 (25) (2026) 12759–12773. doi:10.1007/s11356-026-38111-1.

[23] V. H. Hoang, T. M. P. Nguyen, T. D. Nguyen, T. H. V. Nguyen, T. H. H. Chu, L. P. Hoang, P. Q. Thang, L. H. Nguyen, T. K. Hoang, H.-T. Van, Recycling paper sludge into hydrochar and zno nanocomposite for enhanced ammonium adsorption in aqueous solutions, RSC Advances 15 (9) (2025) 6634–6651. doi:10.1039/d5ra00493d.

[24] L. H. Nguyen, H. T. Van, T. H. H. Chu, T. H. Nguyen, L. P. Hoang, V. A. Hoang, Paper waste sludge-derived hydrochar modified by iron (III) chloride for enhancement of ammonium adsorption: An adsorption mechanism study, Environmental Technology & Innovation 21 (2021) 101223. doi:10.1016/j.eti.2020.101223.

[25] M. Zhang, G. Song, D. L. Gelardi, L. Huang, E. Khan, O. Mašek, S. J. Parikh, Y. S. Ok, Evaluating biochar and its modifications for the removal of ammonium, nitrate, and phosphate in water, Water Research 186 (2020) 116303. doi:10.1016/j.watres.2020.116303.

[26] H. N. Tran, S.-J. You, A. Hosseini-Bandegharaei, H.-P. Chao, Mistakes and inconsistencies regarding adsorption of contaminants from aqueous solutions: A critical review, Water Research 120 (2017) 88–116. doi:10.1016/j.watres.2017.04.014.

[27] E. D. Revellame, D. L. Fortela, W. Sharp, R. Hernandez, M. E. Zappi, Adsorption kinetic modeling using pseudo-first order and pseudo-second order rate laws: A review, Cleaner Engineering and Technology 1 (2020) 100032. doi:10.1016/j.clet.2020.100032.

[28] P. Khaopueak, K. Wechakorn, Hydrothermal carbonization of sucrose into hydrochar: Insights into surface chemistry for efficient removal of cationic dyes, ACS Omega 11 (9) (2026) 14560–14569. doi:10.1021/acsomega.5c10102.

[29] I. Kozyatnyk, V. Benavente, E. Weidemann, F. G. Gentili, S. Jansson, Influence of hydrothermal carbonization conditions on the porosity, functionality, and sorption properties of microalgae hydrochars, Scientific Reports 13 (1) (2023). doi:10.1038/s41598-023-35331-0.

[30] H. Huang, Z. Niu, R. Shi, J. Tang, L. Lv, J. Wang, Y. Fan, Thermal oxidation activation of hydrochar for tetracycline adsorption: the role of oxygen concentration and temperature, Bioresource Technology 306 (2020) 123096. doi:10.1016/j.biortech.2020.123096.

[31] J. A. Villamil, E. Diaz, M. A. de la Rubia, A. F. Mohedano, Potential use of waste activated sludge hydrothermally treated as a renewable fuel or activated carbon precursor, Molecules 25 (15) (2020) 3534. doi:10.3390/molecules25153534.

[32] W. F. Maddams, M. J. Southon, The effect of band width and band shape on resolution enhancement by derivative spectroscopy, Spectrochimica Acta Part A: Molecular Spectroscopy 38 (1982) 459–466. doi:10.1016/0584-8539(82)80022-6.

[33] A. Savitzky, M. J. E. Golay, Smoothing and differentiation of data by simplified least squares procedures., Analytical Chemistry 36 (1964) 1627–1639. doi:10.1021/ac60214a047.

[34] C. Ryan, E. Clayton, W. Griffin, S. Sie, D. Cousens, SNIP, a statistics-sensitive background treatment for the quantitative analysis of PIXE spectra in geoscience applications, Nuclear Instruments and Methods in Physics Research Section B: Beam Interactions with Materials and Atoms 34 (1988) 396–402. doi:10.1016/0168-583X(88)90063-8.

[35] S. Gates-Rector, T. Blanton, The powder diffraction file: a quality materials characterization database, Powder Diffraction 34 (2019) 352–360. doi:10.1017/S0885715619000812.

[36] F. H. Chung, Quantitative interpretation of x-ray diffraction patterns of mixtures. I. matrix-flushing method for quantitative multicomponent analysis, Journal of Applied Crystallography 7 (1974) 519–525. doi:10.1107/s0021889874010375.

[37] A. L. Patterson, The scherrer formula for x-ray particle size determination, Physical Review 56 (1939) 978–982. doi:10.1103/PhysRev.56.978.

[38] C. Spearman, The proof and measurement of association between two things, The American Journal of Psychology 15 (1) (1904) 72–101. doi:10.2307/1412159.

[39] W. H. Kruskal, W. A. Wallis, Use of ranks in one-criterion variance analysis, Journal of the American Statistical Association 47 (260) (1952) 583–621. doi:10.1080/01621459.1952.10483441.

[40] Y. S. Ho, G. McKay, Pseudo-second order model for sorption processes, Process Biochemistry 34 (5) (1999) 451–465. doi:10.1016/s0032-9592(98)00112-5.

[41] H. Akaike, A new look at the statistical model identification, IEEE Transactions on Automatic Control 19 (6) (1974) 716–723. doi:10.1109/tac.1974.1100705.

[42] C. M. Hurvich, C.-L. Tsai, Regression and time series model selection in small samples, Biometrika 76 (1989) 297–307. doi:10.1093/biomet/76.2.297.

[43] I. Langmuir, The adsorption of gases on plane surfaces of glass, mica and platinum, Journal of the American Chemical Society 40 (9) (1918) 1361–1403. doi:10.1021/ja02242a004.

[44] H. Freundlich, Über die adsorption in lösungen, Zeitschrift für Physikalische Chemie 57U (1907) 385–470. doi:10.1515/zpch-1907-5723.

[45] S. Román, J. Libra, N. Berge, E. Sabio, K. Ro, L. Li, B. Ledesma, A. Álvarez, S. Bae, Hydrothermal carbonization: Modeling, final properties design and applications: A review, Energies 11 (2018) 216. doi:10.3390/en11010216.

[46] M. Sevilla, A. Fuertes, Chemical and structural properties of carbonaceous products obtained by hydrothermal carbonization of saccharides, Chemistry – A European Journal 15 (2009) 4195–4203. doi:10.1002/chem.200802097.

[47] R. E. Franklin, Crystallite growth in graphitizing and non-graphitizing carbons, Proceedings of the Royal Society of London. Series A. Mathematical and Physical Sciences 209 (1951) 196–218. doi:10.1098/rspa.1951.0197.

[48] J. Maire, J. Mering, Croissance des dimensions des domaines cristallins au cours de la graphitation du carbone, in: Les Carbones, Pergamon, 1960, pp. 345–350. doi:10.1016/b978-1-4831-9835-4.50046-x.

[49] F. Tuinstra, J. L. Koenig, Raman spectrum of graphite, The Journal of Chemical Physics 53 (1970) 1126–1130. doi:10.1063/1.1674108.

[50] N. Baccile, G. Laurent, F. Babonneau, F. Fayon, M.-M. Titirici, M. Antonietti, Structural characterization of hydrothermal carbon spheres by advanced solid-state MAS 13c NMR investigations, The Journal of Physical Chemistry C 113 (22) (2009) 9644–9654. doi:10.1021/jp901582x.

[51] J. Cai, B. Li, C. Chen, J. Wang, M. Zhao, K. Zhang, Hydrothermal carbonization of tobacco stalk for fuel application, Bioresource Technology 220 (2016) 305–311. doi:10.1016/j.biortech.2016.08.098.

[52] V. P. Chauhan, G. Y. Grobman, N. Vidavsky, J. D. Rimer, Time-resolved dynamics of calcium oxalate dihydrate crystallization, Crystal Growth & Design 24 (2024) 10273–10283. doi:10.1021/acs.cgd.4c01263.

[53] L. A. Currie, Limits for qualitative detection and quantitative determination. application to radiochemistry, Analytical Chemistry 40 (3) (1968) 586–593. doi:10.1021/ac60259a007.

[54] M. T. Reza, J. G. Lynam, M. H. Uddin, C. J. Coronella, Hydrothermal carbonization: Fate of inorganics, Biomass and Bioenergy 49 (2013) 86–94. doi:10.1016/j.biombioe.2012.12.004.

[55] J. Stemann, A. Putschew, F. Ziegler, Hydrothermal carbonization: Process water characterization and effects of water recirculation, Bioresource Technology 143 (2014) 139–146. doi:10.1016/j.biortech.2013.05.098.

[56] Y. Tang, J. Gao, C. Liu, X. Chen, Y. Zhao, Dehydration pathways of gypsum and the rehydration mechanism of soluble anhydrite γ-CaSO4, ACS Omega 4 (2019) 7636–7642. doi:10.1021/acsomega.8b03476.

[57] M. W. Prairie, S. H. Frisbie, K. K. Rao, A. H. Saksri, S. Parbat, E. J. Mitchell, An accurate, precise, and affordable light emitting diode spectrophotometer for drinking water and other testing with limited resources, PLOS ONE 15 (2020) e0226761. doi:10.1371/journal.pone.0226761.

[58] S. M. Moosavi, S. Ghassabian, Linearity of calibration curves for analytical methods: A review of criteria for assessment of method reliability, in: Calibration and Validation of Analytical Methods – A Sampling of Current Approaches, IntechOpen, 2018. doi:10.5772/intechopen.72932.

[59] Y. Zhao, R. Shi, X. Bian, C. Zhou, Y. Zhao, S. Zhang, F. Wu, G. I. N. Waterhouse, L. Wu, C. Tung, T. Zhang, Ammonia detection methods in photocatalytic and electrocatalytic experiments: How to improve the reliability of NH 3 production rates?, Advanced Science 6 (2019) 1802109. doi:10.1002/advs.201802109.

[60] W. P. Utomo, H. Wu, Y. H. Ng, Quantification methodology of ammonia produced from electrocatalytic and photocatalytic nitrogen/nitrate reduction, Energies 16 (2022) 27. doi:10.3390/en16010027.

[61] F. Xiao, A. H. Bedane, J. X. Zhao, M. D. Mann, J. J. Pignatello, Thermal air oxidation changes surface and adsorptive properties of black carbon (char/biochar), Science of The Total Environment 618 (2018) 276–283. doi:10.1016/j.scitotenv.2017.11.008.

© 2026 The Authors | CC-BY 4.0

[62] K. Emerson, R. C. Russo, R. E. Lund, R. V. Thurston, Aqueous ammonia equilibrium calculations: Effect of ph and temperature, Journal of the Fisheries Research Board of Canada 32 (12) (1975) 2379–2383. doi:10.1139/f75-274.

[63] B. Wang, J. Lehmann, K. Hanley, R. Hestrin, A. Enders, Adsorption and desorption of ammonium by maple wood biochar as a function of oxidation and ph, Chemosphere 138 (2015) 120–126. doi:10.1016/j.chemosphere.2015.05.062.

[64] J. Wang, X. Guo, Adsorption isotherm models: Classification, physical meaning, application and solving method, Chemosphere 258 (2020) 127279. doi:10.1016/j.chemosphere.2020.127279.

[65] M. T. Reza, J. Nover, B. Wirth, C. J. Coronella, Hydrothermal carbonization of glucose in saline solution: sequestration of nutrients on carbonaceous materials, AIMS Energy 4 (1) (2016) 173–189. doi:10.3934/energy.2016.1.173.

[66] M. Thommes, K. Kaneko, A. V. Neimark, J. P. Olivier, F. Rodriguez-Reinoso, J. Rouquerol, K. S. W. Sing, Physisorption of gases, with special reference to the evaluation of surface area and pore size distribution (IUPAC technical report), Pure and Applied Chemistry 87 (2015) 1051–1069. doi:10.1515/pac-2014-1117.

[67] J. S. Noh, J. A. Schwarz, Estimation of the point of zero charge of simple oxides by mass titration, Journal of Colloid and Interface Science 130 (1989). doi:10.1016/0021-9797(89)90086-6.

© 2026 The Authors | CC-BY 4.0